INORGANIC CHEMISTRY FRONTIERS

RESEARCH ARTICLE

View Article Online
View Journal | View Issue

Check for updates

Cite this: *Inorg. Chem. Front.*, 2024, **11**, 3418

Magnifying the turn-on luminescence and electrical conductivity *via* the coupling effect of oxidation, metal ion adhesion and pressure within Mn^{II}-MOFs†

Ting-chang Shi,‡[a] Zhi-hui Li,‡[b] Zhiyue Dong,[a] Ming-Hua Zeng *[a,b] and Hai-Bing Xu *[a]

Received 1st March 2024,
Accepted 22nd April 2024

DOI: 10.1039/d4qi00552j

rsc.li/frontiers-inorganic

A metal–organic framework (MOF), Mn^{II}_2-BTDB-MOF (**Mn1**, BTDB = 4,4′-(1,2,5-benzothiadiazole-4,7-diyl) bis-benzoic acid), exhibits enhancement of turn-on luminescence through the restriction of intramolecular vibration (RIV) mechanism, retaining its crystallinity and porosity. As expected, a 1.8-, 3.6-, 45.5-, and 164.4-fold emission enhancement respect to that of **Mn1** by suffering from respective pressure, oxidation, the introduction of Hg^{2+}, and the above three strategies totally, are observed, indicating their coupling effects on luminescence sensor. The results of density functional theory calculations reveal that the introduced metal ions trigger the RIV of BTDB by reducing the changes of the dihedral angle between the ground and excited states, suppressing nonradiative energy exhaustion, and thus magnifying turn-on luminescence. Furthermore, through stepwise fine-tuning the intricate physical and electronic structure associated with oxidation and the introduction of Zn^{2+} under 20 MPa, the electrical resistivity is dramatically improved from $<10^{-17}$ S cm to 4.4×10^{-8} S cm. It is the first time to systematically magnify the luminescence, along with electrical resistivity, by employing the coupling effects of multiple external stimuli on MOFs, thereby highlighting their adaptabilities as sensors and electronics.

Introduction

Stimulus responsive materials (SRMs) respond to environmental changes through chemical and/or structural transformations, triggered by interactions at solid–gas or solid–liquid interfaces.[1] SRMs span from organic polymers to porous inorganic solids, such as metal–organic frameworks (MOFs).[2,3] On the one hand, MOFs can undergo post-synthetic modification (PSM) without compromising the overall framework integrity. On the other hand, the inorganic and the organic moieties, even some guest molecules, within the MOFs, can provide platforms to emit or induce luminescence.[4,5] The recognition/binding events with guest substrates confined by tunable pore sizes and functional pore surfaces, which can be transduced into external optical signals, render MOFs as a new type of luminescent sensing material for the rapid detection of hazardous chemicals at trace concentrations.[6,7] To date, most of the sensing procedures are based on fluorescence quenching, and strategies for the recognition of analytes through turn-on sensing behavior, especially using the coupling effect of more than two stimuli, are scarce.

The luminescence performance of MOFs can be affected by many environmental factors,[8] including physical (pressure)[9] and chemical stimuli (ions,[10–12] solvents,[13–15] pH,[16] gases,[17,18] and more[19–23]). However, unlike other luminescent materials, the intrinsic porosity, large surface area, and strong adsorption affinity of MOFs can effectively enrich guest species. Guest analytes can interact with the host framework through weak van der Waals interactions,[24] hydrogen bonding,[25] and coordination bonds, thus effectively altering the luminescent intensity and/or color of the host by changing its excited-state energy, non-radiation pathway and efficiency.[26]

Herein, we designed a porous Mn^{II}_2-BTDB-MOF (**Mn1**, btdb = 4,4′-(1,2,5-benzothiadiazole-4,7-diyl)bis-benzoic acid) as an SRM based on the restriction of intramolecular vibration

[a] *Ministry-of-Education Key Laboratory for the Synthesis and Application of Organic Functional Molecules, Hubei Collaborative Innovation Center for Advanced Organic Chemical Materials Co-constructed by the Province and Ministry, College of Chemistry and Chemical Engineering, Hubei University, Wuhan 430062, China. E-mail: xhb@hubu.edu.cn, zmh@hubu.edu.cn*

[b] *Department of Chemistry and Pharmaceutical Sciences, Guangxi Normal University, Key Laboratory for the Chemistry and Molecular Engineering of Medicinal Resources, Guilin, 541001, P.R. China*

† Electronic supplementary information (ESI) available: Experimental details, elemental analyses, IR, X-ray crystallography information, UV-Vis spectra, fluorescence spectra. CCDC 2309896. For ESI and crystallographic data in CIF or other electronic format see DOI: https://doi.org/10.1039/d4qi00552j

‡ These authors contributed equally to this work.

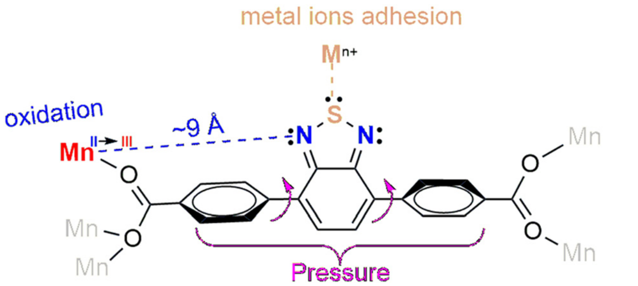

Scheme 1 Strategies for designing metal-BTDB-MOFs with a turn-on sensing behaviour based on the coupling effect of oxidants, metal ions, and pressure.

(RIV) mechanism using the following strategies (Scheme 1): (1) linkers, such as BTDB-containing sulfur or nitrogen atoms as soft bases, favor the anchoring of metal ions, increasing the steric hindrance to suppress the vibration of BTDB;[27] (2) immobilization of the vibrator of BTDB *via* grinding or pressing prevents nonradiative excited energy dissipation;[28] (3) through PSM such as oxidation without perturbing the parent framework;[29] the interactions among metal ions (nodes) and the electron pairs of the adjacent N of BTDB within oxidized MOFs (**Mn1′**) are stronger than those of the original one, thereby magnifying the turn-on luminescence by RIV.[30] As expected, the emission enhancement of **Mn1** suffers from respective stimuli, such as pressure, oxidation, and addition of metal ions, and is much lower than that under multiple stimulus through the RIV mechanism. Density functional theory (DFT) calculations reveal that the introduced metal ions not only decrease the changes in the dihedral angles between the ground and excited states of BTDB, dramatically magnifying the luminescence intensity, but also reduce the band gaps of emissive transitions, red-shifting the emissive bands. Moreover, associated with oxidation, followed by the introduction of Zn^{2+} under 20 MPa, the electrical resistivity is dramatically improved from $<10^{-17}$ S cm to 4.4×10^{-8} S cm. It firstly employs three strategies, synergistically magnifying turn-on luminescence and electrical conductivity, affording great prospects of MOFs as sensors and electronics for environmental applications.

Results and discussion

As shown in Table S1,† although several works based on using BTDB as the linker to construct M-BTDB-MOFs (M = Mn, Pd, Zr) have been reported, due to different components (auxiliary bridging ligand) inducing various coordination modes of metal ions and bridging modes of the linker, the versatile topological structure and porosity of the M-BTDB-MOFs could be provided. For instance, three-dimensional Mn^{II}_4-$BTDB_2$-MOF together with two-dimensional Pb^{II}-BTDB-MOF were previously employed as luminescent sensors for the detection of both highly toxic metal ions, even oxidizing anions with ppb detection limits in solution through luminescence quenching.[31] Also, a luminescent Zr^{IV}_6-$BTDB_2$-MOF exhibits an unprecedented detection limit in aqueous solutions for organic amines with ultralow detection limits, which was driven by hydrogen bonding interactions between the linker and the hosted amines. The selective recognition of different amines depends on their protonation in aqueous, inducing luminescence quenching for aromatic amines, enhancement for aliphatic amine, and negligible changes for pyridine.[32] On the other hand, the in-depth exploration of turn-on sensing behavior through coupling effects within MOFs and its potential on electrical conductivity remain unexplored.

Crystal structure and characterization

The synthetic procedure (Fig. S1†), crystallographic data (Table S2†), selective bond lengths (Table S3†) and angles (Table S4†), together with the crystal structure of **Mn1** (CCDC 2309896†), were analyzed in details. In the structure (Fig. 1a), the Mn^{2+} ion adopts a vacant octahedron coordination with five carboxylate oxygen from five btdb, bridged by carboxylate groups through $\mu^2{:}\eta^1{:}\eta^1{:}\eta^1$ modes, formation of an 1D Mn^{II} chain along the *b* direction, in which the intra Mn⋯Mn distances are within 3.79–5.23 Å, and the intra-chain Mn–μ_2-O–Mn angle is 120.92°. The 1D Mn^{II} chains are linked one to another *via* ligands and construct a 3D framework with various pores, leading to the formation of a wave-like shape along the *a*-axis with the smallest and largest apertures of 3.4 and 4.1 Å, respectively (Fig. S2†). The void volume that is generated after the removal of the coordinating DMF molecules is 25.6% of the total volume, as estimated by PLATON, accommodating lattice guest molecules (Fig. S4†).

After oxidation, the vibrating satellite peak of Mn 2p in the XPS spectrum disappears (Fig. 2b, left), and the binding energy fitted by the Mn 3s orbital shifts to 6.20 eV from 5.40 eV (Fig. 2b, right),[33] confirming that the valence of Mn^{II} in **Mn1** transfers into Mn^{III} in **Mn1′**, broadening and strengthening the vibration in the range of 1300–1604 cm^{-1}, which is attributed to the enhanced strength and symmetry of the coordination bonds between the carboxylate groups and Mn^{3+} (Fig. S3†). Similar PXRD patterns of **Mn1** before and after oxidation, matching the simulated one of single crystal, confirm the chemical stability (Fig. 1c). Combining the results of TG, the desolvated frameworks were generated by heating **Mn1** at 170 °C for 4.5 h and **Mn1′** at 250 °C for 10 h (Fig. S4†); N_2 absorption isotherm under 77 K was used to characterize the porosity of their networks (Fig. S5†), which shows a reversible type II isotherm, indicating the permanent micro-porosity. Gradually increasing the pressure, a little hysteresis between absorption/desorption curves suggests a small amount of meso-porosity in the desolvated material.[34] The saturated uptake is 96.27 and 63.83 cm^3 g^{-1}, and the BET surface area is estimated as 184.66 and 13.07 m^2 g^{-1} for **Mn1** and **Mn1′**, respectively. Through the equation $V_{liq} = P_a \times V_{ads} \times V_m/RT$, the total pore volume is calculated as 1.49×10^{-1} and 9.87×10^{-2} cc g^{-1}, and the pore diameter is less than 1.79 and 1.62 nm at 0.99 atm for **Mn1** and **Mn1′**, respectively. Additionally, the molecular formula of **Mn1′** is deduced as Mn^{III}_2-

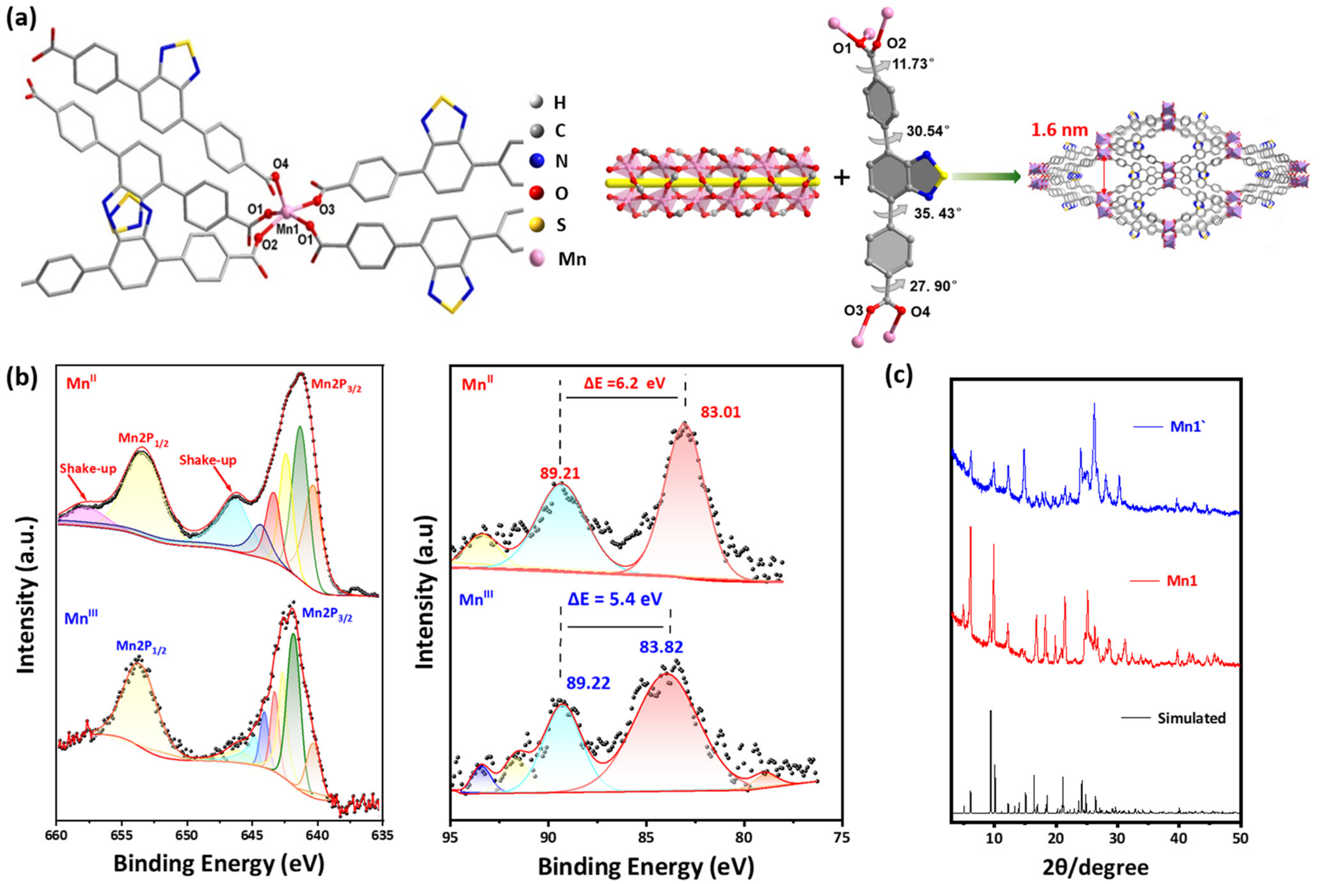

Fig. 1 The asymmetric unit of **Mn1** with the atomic numbering scheme (thermal ellipsoids at 50% probability) (a), and the perspective views of the 3D framework of **Mn1** (b). The corresponding high-resolution XPS spectra of Mn 2p and Mn 3s signal deconvolution and PXRD patterns before and after oxidation (c).

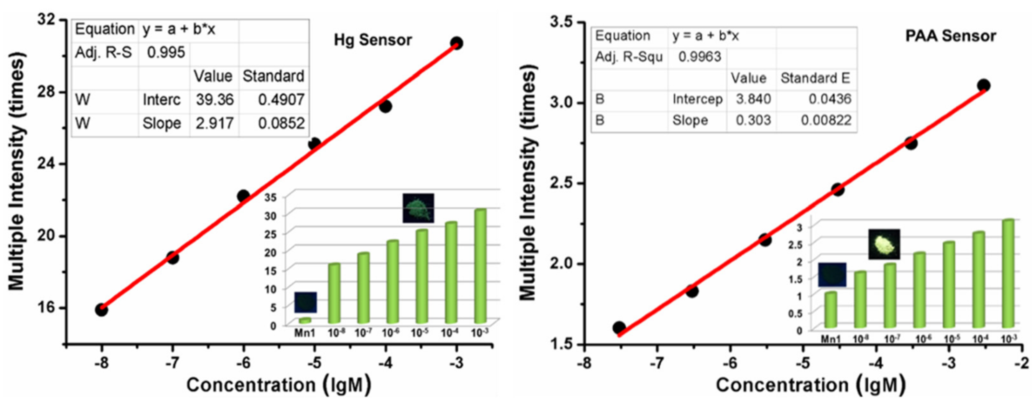

Fig. 2 Rapid detection of PAA (a) and $Hg(ClO_4)_2$ (b) by **Mn1** under UV irradiation with naked-eye limitation.

BTDB·$0.3H_2O$·0.4DMSO·I^- based on the TGA (Fig. S4†) and titration measurement (Fig. S6†).

Optical property

Solid state BTDB and **Mn1** exhibit similar absorption bands at *ca.* 257 nm, 307 nm, and 385 nm, assigned as the π–π* transitions. Upon irradiation within the corresponding absorption bands from 278 to 363 nm, **Mn1** exhibits a green luminescence centered at *ca.* 523 nm, attributed to the π*–π transitions of the ligand (Fig. S7†).

Metal ion sensor. Due to the potential coordination bonding of the free S or N atoms in BTDB, facilitating the sensor performance of metal ions, a series of parallel experiments were set up by immersing **Mn1** crystals into DMF solutions of different metal salts (Ag^+, Zn^{2+}, Hg^{2+}) with the same molar concentrations during the same period, and luminescent tests were conducted on dried solid samples under λ_{ex} = 336 nm, inducing an obvious turn-on luminescence by RIV (Fig. S8†). On the one hand, the typical peaks of PXRD consistent with the simulated one (Fig. S9†) confirm a stable framework during metal ion sensing. On the other hand, since the pore diameters of **Mn1** are much larger than the chosen metal ions, all the introduced metal ions could enter into the pore channel. Neglecting the subtle effect of anions on the luminescence intensity (Fig. S8d†), a more intensive enhancement of luminescent intensity with respect to that of original **Mn1** was observed in perchlorate than that of nitrate (Fig. S8†) since one metal ion would link more than one N/S in different BTDB. Moreover, besides the 19- and 14-times emission enhancement by the introduction of $AgClO_4$/$AgNO_3$ into **Mn1**, the luminescent spectra red shift from 523 nm to 605 nm (Fig. S8a†).

Oxidation sensor. According to a previous work, H_2O_2 was firstly considered as a candidate for **Mn1** oxidation, but different PXRD before and after oxidation indicate the destruction of the original framework integrity (Fig. S10†). Then, the weaker oxidant I_2 was selected to generate Mn′, confirmed by the valence of Mn^{II} to Mn^{III} by XPS (Fig. 1b), with the original framework integrity by similar PXRD (Fig. 1c). The optimal approach came to **Mn1** soaked in a solution of I_2 in DMSO/H_2O (v/v = 1 : 1) (Fig. S11†),[35] where DMSO promotes the dissolution of I_2, and the presence of water induces the reaction $I_2 + H_2O = HI + HIO$. It is the HIO actually as the oxidant that converts Mn^{II} into Mn^{III}, confirmed by the increase in the acidity (Fig. S12†), which magnifies the luminescence intensity to 3.6-times compared with that of **Mn1** (Fig. S13†) due to the stronger interactions between Mn^{III} than Mn^{II} and electron pairs of nitrogen atoms in BTDB, triggering stronger emission intensity under UV irradiation by the RIV mechanism.

Pressure sensor. The powders of **Mn1** trigger turn-on luminescence by RIV under different degrees of pressure, and three things could be found: (i) increasing the pressure on powders up to 40 MPa, 1.8-times luminescence enhancement with respect to that of the original **Mn1** could be achieved (Fig. S14a†); (ii) keeping the pressure at 40 MPa for 5 seconds or lasting or 2 h, the luminescence intensity remains almost unchanged (Fig. S14b†); (iii) the luminescence intensity of **Mn1**′ under 40 MPa significantly magnifies to 21.2 times compared with that of **Mn1** (Fig. S14c†), inducing a bright blue emission under UV irradiation (Fig. S15†).

Two kinds of coupling sensor. According to the above discussion, only 1.8-times luminescence magnification under 40 MPa pressure and a 3.6-fold intensity enhancement relative to that of **Mn1** after oxidation was observed for **Mn1**, whereas the luminescence intensity significantly climbed to 21.2-times compared with those of original **Mn1** under oxidation and 40 MPa pressure. Similarly, 65.7-times luminescence enhancement was obtained by the introduction of $Zn(ClO_4)_2$ into **Mn1**; further, under 40 MPa pressure, 73.3-folds luminescence magnification was observed (Fig. S16a†). Replacing **Mn1** with **Mn1**′, 92.6-times enhancement of luminescence under Zn^{2+} adhesion and 103.7-folds further under 40 MPa pressure appeared (Fig. S16b†). All these facts suggest a coupling effect on the luminescent sensor. Using $AgClO_4$ and $Hg(ClO_4)_2$ instead of $Zn(ClO_4)_2$ in the above experiments, the resultant coupling effect on turn-on luminescence is presented (Fig. S17†). Interestingly, as shown in Table 1, there were some differences dependent on the order. For instance, first oxidation **Mn1** into **Mn1**′, then metal ion adhesion (**MnOM**, M = Ag^+, Zn^{2+}, Hg^{2+}), or introduction of metal ion into **Mn1**, followed by further oxidation (**MnMO**), were studied, and it was found that the coupling effect on turn-on luminescence between **MnOM** and **MnMO** was different, where the latter was slightly more obvious than the former.

Table 1 Relative emission intensity and wavelength of **Mn1** under oxidation, metal ions, pressure (40 MPa) and their coupling sensing at λ_{ex} = 336 nm at room temperature

Factor	RI/ (λ_{em}/nm)	DF	RI/ (λ_{em}/nm)	TF	RI/ (λ_{em}/nm)
Blank	1/523	—	—	—	—
P	1.83/523	O + P	21.2/520	—	—
O	3.64/524	O + Ag^+	22.2/606	O + Ag^+ + P	26.6/606
—	—	O + Hg^{2+}	146.1/544	O + Hg^{2+} + P	164.4/544
—	—	O + Zn^{2+}	92.6/531	O + Zn^{2+} + P	103.7/531
Ag^+	18.7/605	Ag^+ + O	23.9/612	Ag^+ + O + P	26.7/613
Hg^{2+}	47.2/544	Hg^{2+} + O	152.5/544	Hg^{2+} + O + P	158.9/544
Zn^{2+}	65.7/531	Zn^{2+} + O	94.1/531	Zn^{2+} + O + P	104.6/532
Fe^{3+}	8.4/521	Fe^{3+} + O	32.9/515	Fe^{3+} + O + P	59.4/514

RI = relative intensity; DF = double factors; TF = triple factors; O = oxidation by I_2 in DMSO/H_2O, *P* = pressure at 40 MPa, — = none.

Three kinds of coupling sensors. As shown in Table 1, luminescence enhancement occurred from **Mn1** to **MnP**, **MnO** and last **MnOP** of about 1 to 1.8-, 3.6- and finally to 21.2-times; if altering the order from **MnZn** to **MnZnP**, **MnOZn**, and **MnOZnP**, 65.7- to 73.3-, 92.6-, and total 103.7-times luminescence magnification was achieved. Anyway, three kinds of coupling sensors were presented in the above operations, and the total luminescent enhancement slightly depended on the order of the triggers (Fig. S18a†). Interestingly, even the introduction of the famous luminescent quencher of Fe^{3+} into **Mn1**,[36] and further cooperation of oxidation and pressure led to at least 60-times luminescence enhancement (Fig. S18b†), confirming RIV as the dominant mechanism for luminescence enhancement within **Mn1**. For the coupling of oxidation and metal ions adhesion, we deduced that some of the free S in BTDB interacts with the metal ions; such a conclusion was also confirmed by the Raman spectroscopic study in a previous work.[37]

Rapid detection of hazardous chemicals with naked eyes

Fluorescence detection technology with high sensitivity and simple operation has been widely developed.[38,39] Among common toxic heavy metal ions, Hg^{2+} easily causes various diseases, even death.[40] The peroxidation value is usually used as a determination of the quality and deterioration of foods made of fat, such as swill-cooked dirty oil; the higher the peroxidation value, the more the rancidity.[41] Thus, developing a rapid and accurate fluorescence detection approach with naked eyes is significant and important.

As shown in Table 1, luminescence enhancement from **Mn** to **MnO**, **MnOHg** and the last **MnOHgP** is 1- to 3.6-, 146.1-, and finally to 164.4-times; if altering the order from **Mn1** to **MnHg**, **MnHgO**, and **MnHgOP**, 1- to 45.5-, 152.5-, and total 158.9-times luminescence magnification were also observed (Fig. S19a†). All these facts suggest that using **Mn1** as a sensor for Hg^{2+} possesses superior sensitivity. Herein, to realize the quick detection of peroxyacetic acid (PAA) and $Hg(ClO_4)_2$, we carry out the sensing operation by the addition of a drop of hazardous chemicals of DMF solutions into the 10 mg powders. Then, the powders were laid and further dried through filter paper. Under 365 nm UV lamp irradiation, 10^{-7} M for PAA and 10^{-5} M for Hg^{2+} could be easily detected by a bright blue emission with naked eyes (Fig. 2). Also, the consistent PXRD patterns before and after detection (Fig. S9 and 20†) confirmed a stable framework during the sensing procedure. Although such turn-on luminescence for PAA and $Hg(ClO_4)_2$ detection was rapid and sensitivity, the selectivity was still to be solved. Since the introduced metal ions could enter into the channels of Mn1 and they have strong interactions with the electron pairs of adjacent N of BTDB, the cyclic performance of materials under various conditions is inferior (Fig. S21†). Anyway, the rapid detection with ultralow detection limits of **Mn1** with naked eyes is promising for probing the local environment, such as pressure as well as toxic and oxidizing species, which has important environmental and humanitarian implications.

Density functional theory calculations

To further explore the RIV mechanism and the abnormal luminescence enhancement of the quencher Fe^{3+} ions as well as the red-shift phenomenon after introducing Ag^+ ions, we adopted a methodology inspired by previous literature, wherein density functional theory (DFT) calculations were performed on H_2BTDB (H_2L) and $H_2L@Ag^+$/$H_2L@Zn^{2+}$/$H_2L@Fe^{3+}$, respectively (Fig. S22 and Tables S5–12†).[32] The results show that before introducing Zn^{2+}, the dihedral angle between the benzene ring and the thiadiazole group is 38.20° in the ground state and 18.04° in the excited state of H_2L, with a change of 20.16° between the ground and excited states. After introducing Zn^{2+}, the dihedral angle of the ground states decreases to 23.84° and one of the excited states is 21.57°, with a significant reduction of 2.27° (Tables S9 and 10†). This demonstrates that the introduction of Zn^{2+} significantly suppresses the dihedral vibration of H_2L, thus supporting the rationality of the RIV mechanism. As for $H_2L@Fe$, the dihedral angle between the benzene ring and the thiadiazole group is 29.43° in the ground state and 30.17° in the excited state, inducing a change in the dihedral angle that is 0.74° (Tables S11 and 12†) smaller than that in $H_2L@Zn$ (2.27°) (Fig. 3a). On the other hand, the low-lying excited states with similar energy gaps of Fe^{3+} facilitate internal conversion and vibrational relaxation, thus quenching the luminescence. Thus, the cooperation between efficiently preventing RIV and luminescence quenching makes the luminescence enhancement of Fe^{3+}@**Mn1** (8.4 times) lower than that of Zn^{2+}@**Mn1** (65.7 times, Table 1).

Furthermore, the DFT calculations on the frontier molecular orbitals (MOs) of H_2L (Tables S5 and 6†) and $H_2L@Ag^+$ (Tables S7 and 8†) show that the HOMO and LUMO energies are −5.99 eV and −3.34 eV before the addition of Ag^+, giving a band gap of −2.66 eV between the MOs. After the introduction of Ag^+, the HOMO and LUMO energies become −12.44 eV and −9.94 eV, reducing the band gap between MOs to −2.50 eV (Fig. 3b), thus red-shifting the emission bands.

Electrical conductivity modulation

Unlike the previous concept of introducing unpaired electrons into the redox hopping strategy, we emphasize the synergy strategies of both oxidation and guest-promoted transport.[44] Through stepwise fine-tuning the intricate physical and electronic structure,[42,43] a pronounced enhancement of the elec-

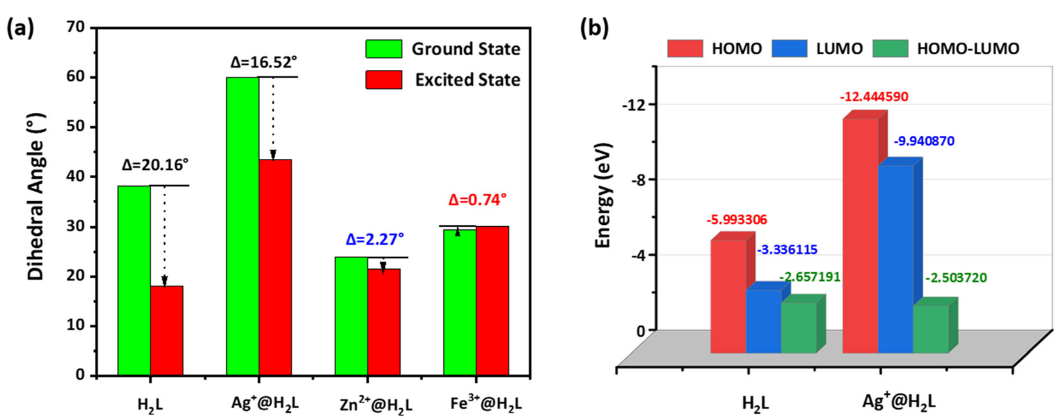

Fig. 3 The angle change (Δ) between the ground state and excited state benzene-thiazole in H_2L (a); the lowest level energy value of the HOMO and LUMO of H_2L and $Ag^+@H_2L$ (b).

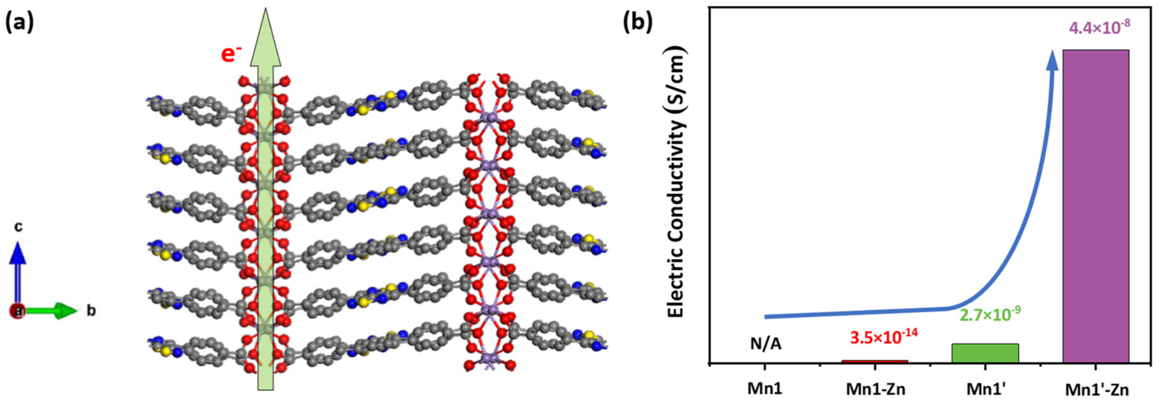

Fig. 4 A-axis-aligned 2D structure of **Mn1** (a), and conductivity of **Mn1** under Zn^{2+} adhesion/oxidation spectra (b).

tric conductivity of **Mn1** upon oxidation and subsequent introduction of metal ions was observed. On the one hand, the d-electron configuration of Mn^{2+} in **Mn1** is fully occupied, without unpaired electrons. After oxidation, the Mn^{3+} in **Mn1′** creates an unpaired electron, which participates in electron conduction along with the *c*-axis of the lattice, thus magnifying the electrical conductivity (Fig. 4a). On the other hand, according to the hard–soft acid–base theory, Zn^{2+} being a relatively soft metal ion easily experiences π-d conjugated bonds with the softer S or N atoms in BTDB, further optimizing the electrical conductivity.

As shown in Fig. 4b and Tables S13–15,† the value of resistance of **Mn1** exceeds the maximum range of our high-impedance meter with a maximum detection limit of 10^{17} Ω cm. Excluding the effect of adsorbed I_2 for electrical conductivity (Fig. S23†), after the oxidation of **Mn1** into **Mn1′** under a pressure of 20 MPa, the electrical conductivity reaches 2.68 × 10^{-9} S cm^{-1}. On the further introduction of Zn^{2+} into **Mn1′** then under 20 MPa, it climbs up to 4.4 × 10^{-8} S cm^{-1} (Fig. S24–26†). The above findings highlight the remarkably tunable effect of Mn-MOF on the conductivity under different chemical environments, bolstering their potential applications in sensing circuits and other electronic domains.[45]

Conclusions

We designed a porous Mn_2^{II}-BTDB-MOFs (**Mn1**) as SRMs based on the RIV mechanism with its original crystallinity and porosity to realize turn-on luminescence through the coupling effect among oxidation, metal ions adhesion and pressure. Since magnifying the luminescence by the coupled stimulus is much higher than that by the respective one, the rapid detection of Hg^{2+} by naked eyes with ultralow detection limits is operative and practicable. Benefiting from the smallest changes in the dihedral angle, which effectively prevents non-radiative energy exhaustion by RIV, an obvious enhancement of turn-on luminescence still could be observed by the introduction of the luminescence quencher of Fe^{3+}. Also, the introduced metal ions lower the band gaps of emissive transitions, red-shifting the emission band by the introduction of Ag^{+}. Beside magnifying the turn-on luminescence, we also dramatically improved the electrical conductivity of **Mn1** by the above coupled stimulus, highlighting the adaptability of MOFs in diverse external stimulus, which is beneficial for applications of sensors and electronics.

Conflicts of interest

There are no conflicts to declare.

Acknowledgements

We thank the financial support from BAGUI talent program in Guangxi Province (no. 2019AC26001), the NSFC (no. 22273019, 22171075, U23A2080); National Natural Science Foundation of China for Distinguished Young Scholars (no. 22101077), the Youth Foundation of Hubei Province (no. 2021CFB092), the "Chu-Tian Scholar" Program of Hubei Province, and Wuhan Science and Technology (2023010201010136).

References

1 A. Muñoz-Bonilla, M. Fernández-García and J. Rodríguez-Hernández, Towards hierarchically ordered functional porous polymeric surfaces prepared by the breath figures approach, *Prog. Polym. Sci.*, 2014, **39**, 510–554.
2 S. Mandal, S. Natarajan, P. Mani and A. Pankajakshan, Post-Synthetic Modification of Metal–Organic Frameworks Toward Applications, *Adv. Funct. Mater.*, 2020, **31**, 2006291.
3 K. Müller-Buschbaum, F. Beuerle and C. Feldmann, MOF based luminescence tuning and chemical/physical sensing, *Microporous Mesoporous Mater.*, 2015, **216**, 171–199.
4 L. Chen, R. Luque and Y. Li, Controllable design of tunable nanostructures inside metal-organic frameworks, *Chem. Soc. Rev.*, 2017, **46**, 4614–4630.

5 Y. Liu, X. Y. Xie, C. Cheng, Z. S. Shao and H. S. Wang, Strategies to fabricate metal–organic framework (MOF)-based luminescent sensing platforms, *J. Mater. Chem. C*, 2019, **7**, 10743–10763.
6 M. Woellner, S. Hausdorf, N. Klein, P. Mueller, M. W. Smith and S. Kaskel, Adsorption and Detection of Hazardous Trace Gases by Metal-Organic Frameworks, *Adv. Mater.*, 2018, **30**, e1704679.
7 G. L. Yang, X. L. Jiang, H. Xu and B. Zhao, Applications of MOFs as Luminescent Sensors for Environmental Pollutants, *Small*, 2021, **17**, e2005327.
8 X. D. Zhu, K. Zhang, Y. Wang, W. W. Long, R. J. Sa, T. F. Liu and J. Lu, Fluorescent Metal-Organic Framework (MOF) as a Highly Sensitive and Quickly Responsive Chemical Sensor for the Detection of Antibiotics in Simulated Wastewater, *Inorg. Chem.*, 2018, **57**, 1060–1065.
9 I. E. Collings and A. L. Goodwin, Metal–organic frameworks under pressure, *J. Appl. Phys.*, 2019, **126**, 181101.
10 S. S. Zhao, J. Yang, Y. Y. Liu and J. F. Ma, Fluorescent Aromatic Tag-Functionalized MOFs for Highly Selective Sensing of Metal Ions and Small Organic Molecules, *Inorg. Chem.*, 2016, **55**, 2261–2273.
11 X. Song, T. K. Kim, H. Kim, D. Kim, S. Jeong, H. R. Moon and M. S. Lah, Post-Synthetic Modifications of Framework Metal Ions in Isostructural Metal–Organic Frameworks: Core–Shell Heterostructures via Selective Transmetalations, *Chem. Mater.*, 2012, **24**, 3065–3073.
12 J. Zhao, Y. N. Wang, W. W. Dong, Y. P. Wu, D. S. Li and Q. C. Zhang, A Robust Luminescent Tb(III)-MOF with Lewis Basic Pyridyl Sites for the Highly Sensitive Detection of Metal Ions and Small Molecules, *Inorg. Chem.*, 2016, **55**, 3265–3271.
13 F. Millange, C. Serre, N. Guillou, G. Férey and R. I. Walton, Structural Effects of Solvents on the Breathing of Metal–Organic Frameworks: An In Situ Diffraction Study, *Angew. Chem.*, 2008, **120**, 4168–4173.
14 B. Chen, X. Wang, Q. Zhang, X. Xi, J. Cai, H. Qi, S. Shi, J. Wang, D. Yuan and M. Fang, Synthesis and characterization of the interpenetrated MOF-5, *J. Mater. Chem. A*, 2010, **20**, 3758–3767.
15 Y. Wu, G. P. Yang, Y. Zhao, W. P. Wu, B. Liu and Y. Y. Wang, Three new solvent-directed Cd(II)-based MOFs with unique luminescent properties and highly selective sensors for Cu^{2+} cations and nitrobenzene, *Dalton Trans.*, 2015, **44**, 3271–3277.
16 M. Ding, X. Cai and H. L. Jiang, Improving MOF stability: approaches and applications, *Chem. Sci.*, 2019, **10**, 10209–10230.
17 M. Alhamami, H. Doan and C. H. Cheng, A Review on Breathing Behaviors of Metal-Organic-Frameworks (MOFs) for Gas Adsorption, *Materials*, 2014, **7**, 3198–3250.
18 J. R. Li, R. J. Kuppler and H. C. Zhou, Selective gas adsorption and separation in metal-organic frameworks, *Chem. Soc. Rev.*, 2009, **38**, 1477–1504.
19 W. Fan, X. Zhang, Z. Kang, X. Liu and D. Sun, Iso-reticular chemistry within metal–organic frameworks for gas storage and separation, *Coord. Chem. Rev.*, 2021, **443**, 213968.
20 K. I. Hadjiivanov, D. A. Panayotov, M. Y. Mihaylov, E. Z. Ivanova, K. K. Chakarova, S. M. Andonova and N. L. Drenchev, Power of Infrared and Raman Spectroscopies to Characterize Metal-Organic Frameworks and Investigate Their Interaction with Guest Molecules, *Chem. Rev.*, 2021, **121**, 1286–1424.
21 H. Li, L. Li, R.-B. Lin, W. Zhou, Z. Zhang, S. Xiang and B. Chen, Porous metal-organic frameworks for gas storage and separation: Status and challenges, *J. Energy Chem.*, 2019, **1**, 100006.
22 E. V. Perez, K. J. Balkus, J. P. Ferraris and I. H. Musselman, Mixed-matrix membranes containing MOF-5 for gas separations, *J. Membr. Sci.*, 2009, **328**, 165–173.
23 J.-H. Wang, M. Li and D. Li, A dynamic, luminescent and entangled MOF as a qualitative sensor for volatile organic solvents and a quantitative monitor for acetonitrile vapour, *Chem. Sci.*, 2013, **4**, 1793–1801.
24 R. Poloni, B. Smit and J. B. Neaton, CO_2 capture by metal-organic frameworks with van der Waals density functionals, *J. Phys. Chem. A*, 2012, **116**, 4957–4964.
25 I. Ahmed and S. H. Jhung, Applications of metal-organic frameworks in adsorption/separation processes via hydrogen bonding interactions, *Chem. Eng. J.*, 2017, **310**, 197–215.
26 P. Deria, J. Yu, T. Smith and R. P. Balaraman, Ground-State versus Excited-State Interchromophoric Interaction: Topology Dependent Excimer Contribution in Metal-Organic Framework Photophysics, *J. Am. Chem. Soc.*, 2017, **139**, 5973–5983.
27 L. Zhu, B. Zhu, J. Luo and B. Liu, Design and Property Modulation of Metal–Organic Frameworks with Aggregation-Induced Emission, *ACS Mater. Lett.*, 2020, **3**, 77–89.
28 C. X. Chen, S. Y. Yin, Z. W. Wei, Q. F. Qiu, N. X. Zhu, Y. N. Fan, M. Pan and C. Y. Su, Pressure-Induced Multiphoton Excited Fluorochromic Metal-Organic Frameworks for Improving MPEF Properties, *Angew. Chem., Int. Ed.*, 2019, **58**, 14379–14385.
29 Z. Yin, S. Wan, J. Yang, M. Kurmoo and M. H. Zeng, Recent advances in post-synthetic modification of metal–organic frameworks: New types and tandem reactions, *Coord. Chem. Rev.*, 2019, **378**, 500–512.
30 Y. Y. Liu, X. Zhang, K. Li, Q. C. Peng, Y. J. Qin, H. W. Hou, S. Q. Zang and B. Z. Tang, Restriction of Intramolecular Vibration in Aggregation-Induced Emission Luminogens: Applications in Multifunctional Luminescent Metal-Organic Frameworks, *Angew. Chem., Int. Ed.*, 2021, **60**, 22417–22423.
31 A. K. Jana and S. Natarajan, Fluorescent Metal–Organic Frameworks for Selective Sensing of Toxic Cations (Tl^{3+}, Hg^{2+}) and Highly Oxidizing Anions ($(CrO_4)^{2-}$, $(Cr_2O_7)^{2-}$, $(MnO_4)^{-}$), *ChemPlusChem*, 2017, **82**, 1153–1163.
32 A. Mallick, A. M. El-Zohry, O. Shekhah, J. Yin, J. Jia, H. Aggarwal, A.-H. Emwas, O. F. Mohammed and M. Eddaoudi, Unprecedented Ultralow Detection Limit of Amines using a Thiadiazole-Functionalized Zr(IV)-Based

Metal–Organic Framework, *J. Am. Chem. Soc.*, 2019, **141**, 7245–7249.

33 M. C. Biesinger, B. P. Payne, A. P. Grosvenor, L. W. M. Lau, A. R. Gerson and R. S. C. Smart, Resolving surface chemical states in XPS analysis of first row transition metals, oxides and hydroxides: Cr, Mn, Fe, Co and Ni, *Appl. Surf. Sci.*, 2011, **257**, 2717–2730.

34 X. Y. Tian, H. L. Zhou, X. W. Zhang, C. Wang, Z. H. Qiu, D. D. Zhou and J. P. Zhang, Two Isostructural Flexible Porous Coordination Polymers Showing Contrasting Single-Component and Mixture Adsorption Properties for Propylene/Propane, *Inorg. Chem. Commun.*, 2020, **59**, 6047–6052.

35 M. H. Zeng, Z. Yin, Y. X. Tan, W. X. Zhang, Y. P. He and M. Kurmoo, Nanoporous cobalt(II) MOF exhibiting four magnetic ground states and changes in gas sorption upon post-synthetic modification, *J. Am. Chem. Soc.*, 2014, **136**, 4680–4688.

36 R. R. Srivastava, V. K. Singh and A. Srivastava, Facile synthesis of highly fluorescent water-soluble SnS_2 QDs for effective detection of Fe^{3+} and unveiling its fluorescence quenching mechanism, *Opt. Mater. Express*, 2020, **109**, 110337.

37 P. Rodríguez-Zamora, C. A. Cordero-Silis, J. Fabila, J. C. Luque-Ceballos, F. Buendía, A. Heredia-Barbero and I. L. Garzón, Interaction Mechanisms and Interface Configuration of Cysteine Adsorbed on Gold, Silver, and Copper Nanoparticles, *Langmuir*, 2022, **38**, 5418–5427.

38 A. Karmakar, P. Samanta, S. Dutta and S. K. Ghosh, Fluorescent "Turn-on" Sensing Based on Metal-Organic Frameworks (MOFs), *Chem. – Asian J.*, 2019, **14**, 4506–4519.

39 D. Zhao, S. Yu, W. J. Jiang, Z. H. Cai, D. L. Li, Y. L. Liu and Z. Z. Chen, Recent Progress in Metal-Organic Framework Based Fluorescent Sensors for Hazardous Materials Detection, *Molecules*, 2022, **27**, 2226.

40 R. A. Bernhoft, Mercury toxicity and treatment: a review of the literature, *J. Environ. Public Health*, 2012, **2012**, 460508.

41 J. Kanner, Oxidative processes in meat and meat products: Quality implications, *Meat Sci.*, 1994, **36**, 169–189.

42 A. Gładysiak, T. N. Nguyen, M. Spodaryk, J. H. Lee, J. B. Neaton, A. Züttel and K. C. Stylianou, Incarceration of Iodine in a Pyrene–Based Metal–Organic Framework, *Chem. – Eur. J.*, 2018, **25**, 501–506.

43 X. Zhang, I. da Silva, R. Fazzi, A. M. Sheveleva, X. Han, B. F. Spencer, S. A. Sapchenko, F. Tuna, E. J. L. McInnes, M. Li, S. Yang and M. Schröder, Iodine Adsorption in a Redox-Active Metal–Organic Framework: Electrical Conductivity Induced by Host–Guest Charge-Transfer, *Inorg. Chem.*, 2019, **58**, 14145–14150.

44 L. S. Xie, G. Skorupskii and M. Dinca, Electrically Conductive Metal-Organic Frameworks, *Chem. Rev.*, 2020, **120**, 8536–8580.

45 E. M. Johnson, S. Ilic and A. J. Morris, Design Strategies for Enhanced Conductivity in Metal-Organic Frameworks, *ACS Cent. Sci.*, 2021, **7**, 445–453.